

Numerical simulation of a concentrated emulsion in shear flow

By M. LOEWENBERG[†] AND E. J. HINCH

Department of Applied Mathematics and Theoretical Physics, The University of Cambridge,
Silver Street, Cambridge CB3 9EW, UK

(Received 22 August 1995 and in revised form 14 February 1996)

A three-dimensional computer simulation of a concentrated emulsion in shear flow has been developed for low-Reynolds-number finite-capillary-number conditions. Numerical results have been obtained using an efficient boundary integral formulation with periodic boundary conditions and up to twelve drops in each periodically replicated unit cell. Calculations have been performed over a range of capillary numbers where drop deformation is significant up to the value where drop breakup is imminent. Results have been obtained for dispersed-phase volume fractions up to 30% and dispersed- to continuous-phase viscosity ratios in the range of 0 to 5. The results reveal a complex rheology with pronounced shear thinning and large normal stresses that is associated with an anisotropic microstructure that results from the alignment of deformed drops in the flow direction. The viscosity of an emulsion is only a moderately increasing function of the dispersed-phase volume fraction, in contrast to suspensions of rigid particles or undeformed drops. Unlike rigid particles, deformable drops do not form large clusters.

1. Introduction

Emulsions are viscous microstructured fluids that arise in a wide range of industrial applications including advanced materials processing, waste treatment, enhanced oil recovery, food processing, and pharmaceutical manufacturing (Lissant 1984; Friberg 1976; D'Arrigo 1986; Sjöblom 1992). In these applications, it is often necessary to predict or manipulate the rheology of an emulsion or its microstructure. Recently, for instance, there has been considerable interest in incompatible polymer blends because of the attractive mechanical properties that can be achieved and because of the need for recycling plastics (Roetting & Hinrichsen 1994; Teh, Rudin & Keung 1994). Processing these materials requires a detailed rheological knowledge of their emulsified melts and the mechanical properties of the finished products are largely determined by the microstructure of their melts.

In a low-Reynolds-number shear flow, emulsion rheology is determined by the volume fraction of the dispersed phase, ϕ , the dispersed- to continuous-phase viscosity ratio, λ , and the capillary number, $Ca = \mu \dot{\gamma} a / \sigma$, where $\dot{\gamma}$ is the imposed shear rate, a is the undeformed drop radius, μ is the continuous-phase viscosity, and σ is the interfacial tension. The capillary number determines the qualitative importance of drop deformation and is evidently a dimensionless shear rate formed from the ratio of

[†] Present address: Department of Chemical Engineering, Yale University, New Haven, Connecticut 06520-2159, USA.

deforming viscous stresses to the restoring influence of interfacial tension. Surfactants and polydispersity introduce additional parameters that will not be discussed in the present article.

A vast body of literature reflects the active interest in emulsion rheology. Owing to the complexity of the problem, however, there has been limited progress towards a fundamental basis for understanding and predicting the rheology of concentrated emulsions. Instead, empirical correlations have been widely used to predict rheological behaviour (e.g. Pal & Rhodes 1985, 1989); as expected, however, they are unreliable beyond the original data upon which they are based. Simplified microphysical models have also been developed that can provide valuable physical insights (e.g. Schwartz & Princen 1987; Doi & Ohta 1991; Das *et al.* 1992). Unfortunately, detailed calculations are unavailable for guiding the development of these models and carefully testing the validity of their *ad hoc* assumptions; the reliability of these models is therefore unknown.

Difficulties encountered in early experimental studies were overcome by Princen & Kiss (1989) with a novel experimental procedure for obtaining and interpreting reliable rheological measurements in concentrated emulsions using a wide-gap Couette viscometer. In their oft-cited article, Princen & Kiss (1989) outline several specific requirements for the Couette viscometer and the finely dispersed test emulsions used in their study. They intentionally eliminated the complicating effects of drop deformation and drop breakup by restricting their study to conditions characterized by very small capillary numbers, $Ca < 10^{-4}$. More recently, several other groups have used similar procedures to obtain high-quality rheological measurements in concentrated emulsions (e.g. Otsubo & Prud'homme 1994). However, most of these studies continue to focus on vanishingly small capillary number conditions where drop deformation is unimportant; unfortunately, the concentrated microemulsions designed for experimental studies do not adequately represent all of the emulsions that arise in practice. In concentrated emulsions, under conditions where drop deformation is significant, interpretation of experimental measurements must rely on untested conjectures (e.g. Benali 1993; Aronson & Petko 1993), phenomenological models (e.g. Doi & Ohta 1991), or theories (Choi & Schowalter 1975) and numerical computations (de Bruin 1989; Kennedy, Pozrikidis & Skalak 1994) for dilute emulsions. The interpretation of drop deformation effects on the rheology of a concentrated emulsion is an open question.

A rigorous numerical simulation of concentrated emulsion flow is needed to fully and reliably interpret rheological measurements in terms of the detailed emulsion microstructure, to broaden the accessible range of conditions that can be used for meaningful experimental studies, and to predict the rheology and microstructure under conditions that are adverse for experimentation. Numerical simulations would also provide an essential tool for guiding the construction of statistical microphysical models and a precise instrument to gauge their validity. Recently, several numerical descriptions have been developed that focus on various essential aspects of emulsion flow. Zinchenko (1984) developed an elegant semi-dilute theory for conditions where drop deformation is negligible. Mo & Sangani (1994) used a generalized Stokesian dynamics approach to describe the hydrodynamic interactions between fixed random configurations of spherical drops in a concentrated emulsion. Zhou & Pozrikidis (1993, 1994) constructed numerical simulations using boundary integral calculations that describe the flow of a two-dimensional disordered emulsion with deformable drops using twelve drops with periodic boundary conditions. Li, Zhou & Pozrikidis (1995) and Pozrikidis (1993) performed boundary integral calculations for shear flow

of two- and three-dimensional ordered lattices of deformable drops with the same viscosity as the continuous-phase fluid.

The foregoing investigations have revealed a wealth of interesting rheological and microstructural features that provide qualitative insights into concentrated emulsions which are consistent with certain qualitative observations. These studies motivate further effort towards a realistic numerical simulation of concentrated emulsion flow, presumably a description that incorporates the essential features of the disordered and dynamically changing three-dimensional microstructure. Unfortunately, the foregoing simulations are computationally limited according to Pozrikidis (1993); he reports that his three-dimensional single-drop calculations require 44 CPU hours on a supercomputer even though his results were restricted to transient (strains up to 4), rather than steady-state behaviour and to the special case of drops with the same viscosity as the continuous-phase fluid ($\lambda = 1$). Therefore a simple generalization of Pozrikidis (1993) is impractical: a description of a disordered emulsion with twelve drops per unit cell would require several CPU years on a supercomputer because the computation time scales with the number of drops squared and the four-fold symmetry for an ordered lattice is lost for disordered configurations. Considerably more computation time would be required to obtain steady-state results and results for drops with a viscosity different from the continuous-phase fluid ($\lambda \neq 1$).

In this article, we describe an efficient numerical simulation that incorporates a disordered dynamic microstructure, yet circumvents the foregoing computational obstacles. Using our simulation, steady-state rheological behaviour can be computed for concentrated emulsions with differing disperse- and continuous-phase viscosities ($\lambda \neq 1$) in only a few hours on an ordinary workstation using up to twelve drops in each periodically replicated cell. The numerical simulation is described in §2, numerical results are presented in §3, steady-state results in §4, and concluding remarks are given in §5.

2. Numerical simulation

2.1. Surface discretization and curvature calculation

In anticipation of the boundary integral formulation, described below, the interfaces of the drops were triangulated by subdividing the edges of an icosahedron into n equal segments, thereby forming the subtriangles on each face of an icosahedron as shown in figure 1(a). The additional vertices are displaced radially outward onto the spherical surface that circumscribes the icosahedron. By this procedure, the drop surface is discretized into $N = 20n^2$ flat triangles of roughly equal area. All of the $\frac{1}{2}N + 2$ vertices have coordination number 6 except for the evenly spaced icosahedron vertices that have coordination number 5. In hindsight, a still better procedure would involve interchangeable vertex connections but this has not been implemented nor would it be advantageous for most of the simulations that we have attempted.

The curvature was computed at vertices by the formula

$$\kappa n \Delta S \approx \int_{\Delta S} (\nabla \cdot \mathbf{n}) \mathbf{n} dA = - \int_C \mathbf{t} dl, \quad (2.1)$$

where κ is the mean curvature, C is the path that passes through the bisectors of the triangle edges surrounding a vertex, ΔS is the area enclosed by C , \mathbf{n} is the outward normal to the surface, and \mathbf{t} is a unit vector that is tangent to the triangle faces and perpendicular to C , as depicted in figure 1(b).

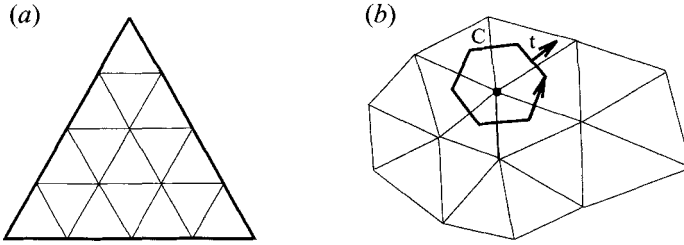


FIGURE 1. Surface discretization and curvature calculation: (a) subdiscretization of icosahedron face ($n = 4$); (b) line integration for curvature calculation at a vertex.

We found this procedure for computing curvature simpler to implement and generally more accurate than other local methods (e.g. fitting a locally quadratic or ellipsoidal surface), as explained below. Global descriptions that involve fitting a coordinate system are unattractive because they necessarily result in closely spaced collocation points near the coordinate singularities. According to the stability requirement for time integration, discussed below, this requires proportionally shorter time integration steps and longer computation times. The spectral boundary element representation of Muldowney & Higdon (1995) is much more accurate but requires much longer computation times.

The separation between vertices is $O(1/N^{1/2})$ on a surface embedded in three dimensions. Errors in the normal vector and integrals of the curvature on elements of area ΔS are only accurate to this order, as (2.1) illustrates because t depends on the orientation of a flat triangular face. Formula (2.1) is exact for a sphere but calculations for spheroids and more complex spool-shaped (quartic) surfaces reveal that it has an average error $\approx 6/N^{1/2}$. Generally, other local methods fare slightly worse because they are less localized, therefore less able to describe rapid variations in curvature. This pessimistic conclusion seems to be an intrinsic feature of curvature calculations on surfaces in three dimensions. Fortunately, curvature errors are reduced because of the conservation principle that underlies (2.1), as explained at the end of §2.2. The use of flat triangular elements introduces a higher-order, $O(1/N)$ surface-area error; evidently, curved boundary elements are an unnecessary refinement.

According to the boundary integral formulation vertices are convected with the local fluid velocity, as implied by (2.6). As a result, a universal difficulty with boundary integral calculations is the tendency for the spacing between points to become highly irregular after a short simulation time. This effect is slightly lessened, but not eliminated, by convecting the points with the normal component of the fluid velocity, $(\mathbf{u} \cdot \mathbf{n})\mathbf{n}$. We were able to fully control the grid and eliminate unwanted grid distortion by convecting the points with a velocity $\mathbf{v} = \mathbf{u} + \mathbf{w}$, where \mathbf{u} is the fluid velocity computed by boundary element calculations, according to (2.3), and \mathbf{w} is a locally defined tangential ‘velocity’ field that maintains the desired distribution of points on the drop surfaces. We defined this tangential velocity field at a vertex \mathbf{x}^i by a rule involving only vertices directly connected to \mathbf{x}^i

$$\mathbf{w}^i = \frac{N^{3/2}}{300} \frac{1}{1 + \lambda} (\mathbf{I} - \mathbf{nn}) \sum_j \left[1 + 4 \frac{|\mathbf{x}^j - \mathbf{x}^i|}{h(\mathbf{x}^j)} + |\kappa_j|^{3/2} \right] \Delta S_j (\mathbf{x}^j - \mathbf{x}^i), \quad (2.2)$$

where $h(\mathbf{x}^j)$ is the minimum distance between \mathbf{x}^j and another drop surface. The above rule maintains a uniform grid with a somewhat higher density of points in near-contact regions between drop surfaces and on regions of high curvature. The

same rule was used for all computations described in this article and, in all cases, a well-controlled grid was maintained. However, our experience indicates that the precise local rule that defines w^i is unimportant; careful optimization is unnecessary.

2.2. Boundary integral formulation

The velocity was computed at collocation points, taken as the vertices of our discretization grid, by a modified version of the second-kind boundary integral formulation developed by Rallison & Acrivos (1978) and Rallison (1981) for deformable drops. After eliminating the troublesome integrand singularities and generalizing their result to M distinct drops periodically replicated in three-dimensional space, the result is

$$\begin{aligned}
 (\lambda + 1) \mathbf{u}(\mathbf{x}_0) = & 2Ca(x_{2,0}, 0, 0) + (\lambda - 1) \mathbf{u}(\mathbf{x}_0) - \frac{1}{4\pi} \sum_{j=1}^M \int_{S_j(\mathbf{x})} [(\kappa(\mathbf{x}) - \kappa(\mathbf{x}^*)) \mathbf{G}(\hat{\mathbf{x}}) \cdot \mathbf{n}(\mathbf{x}) \\
 & + (\lambda - 1) [\mathbf{u}(\mathbf{x}) - \mathbf{u}(\mathbf{x}^*)] \cdot \mathbf{T}(\hat{\mathbf{x}}) \cdot \mathbf{n}(\mathbf{x})] d\mathbf{x}, \quad (2.3)
 \end{aligned}$$

where \mathbf{x}_0 is a collocation point on one of the drop surfaces, $x_{2,0}$ is the coordinate in the direction of the velocity gradient as shown in figure 2, and $\hat{\mathbf{x}} = \mathbf{x} - \mathbf{x}_0$. Equation (2.3) has been made dimensionless using a and σ/μ for the characteristic length and velocity. The kernel functions \mathbf{G} and \mathbf{T} are discussed in the following subsection.

Polydisperse effects from drops with different sizes, a_j , are incorporated in (2.3). Drops with differing viscosities can be accommodated by subscripting the viscosity ratio: λ_j inside the integral term and λ_i outside the integral term, where $S_i(\mathbf{x})$ contains \mathbf{x}_0 . The effect of a short-range interaction potential between drops and the effects of drops with different excess densities $\Delta\rho_j$, or different surface tensions σ_j can be incorporated by simply replacing $\kappa(\mathbf{x})$ in (2.3) with

$$f(\mathbf{x}) = \left(\frac{\sigma_j}{\sigma_1} \right) \kappa(\mathbf{x}) - \left(\frac{\Delta\rho_j a_j^3}{\Delta\rho_1 a_1^3} \right) Bo(\mathbf{g} \cdot \mathbf{x}) + Hg[h(\mathbf{x})] \quad (2.4)$$

where $g(h)$ is a dimensionless short-range function of the local distance to another drop surface, $h(\mathbf{x})$. The potential parameter $H = A/\sigma_1 a_1^2$, the Bond number $Bo = \Delta\rho_1 a_1^2 g/\sigma_1$, and the capillary number $Ca = \mu\dot{\gamma} a_1/\sigma_1$ are defined by the physical properties of an arbitrarily selected reference drop (labelled 1) and A characterizes the strength of the short-range interaction potential. Unfortunately, the tangential Marangoni stresses associated with surfactant concentration gradients on the drop surfaces cannot be as simply incorporated into the above formulation. In this article, we show some results that were obtained using a stabilizing short-range repulsion but otherwise do not use these generalizations: a monodisperse neutral density ($Bo = 0$) emulsion is henceforth assumed.

According to (2.3), the velocity at each collocation point requires integration over every drop surface, $j = 1, \dots, M$ within the unit cell. The singularity-subtracted formulation was derived using the identities (Pozrikidis 1992, pp. 20,21),

$$\int_{S_j(\mathbf{x})} \mathbf{G}(\hat{\mathbf{x}}) \cdot \mathbf{n}(\mathbf{x}) d\mathbf{x} = 0; \quad - \int_{S_j(\mathbf{x})} \mathbf{T}(\hat{\mathbf{x}}) \cdot \mathbf{n}(\mathbf{x}) d\mathbf{x} = \begin{cases} 4\pi \mathbf{I}, & \mathbf{x}^* \text{ on } S_j(\mathbf{x}) \\ 0, & \mathbf{x}^* \text{ on } S_i(\mathbf{x}), i \neq j. \end{cases}$$

For integration on the drop surface containing \mathbf{x}_0 , we set $\mathbf{x}^* = \mathbf{x}_0$ in (2.3); for integration on the remaining drop surfaces, \mathbf{x}^* is the collocation point on the surface that is *closest* to \mathbf{x}_0 . This procedure removes the integrand singularities that arise

from small separations between drop surfaces and the singularities on the surface that contains the collocation point, \mathbf{x}_0 . Regularizing the integrand by singularity subtraction greatly simplifies the numerical integration requirements: surface integrals can be performed with integrand evaluations only at the collocation points; the contribution from the boundary element containing \mathbf{x}_0 is $O(1/N)$ and therefore negligible at this order. The $O(1/N)$ error introduced by this simple trapezoid-rule surface integration procedure is generally smaller than the error introduced by the curvature calculation, discussed in §2.1. Higher-order surface integration rules are therefore unnecessary.

Fortunately, the error introduced by the curvature calculation is reduced by the singularity subtraction. As a result of this integrand regularization, velocities computed from (2.3) depend on more evenly weighted integrals of the curvature that are more accurate because of the conservation principle that underlies (2.1): over an entire drop surface, integrals of the curvature vanish exactly because of line integral cancellation. Similarly, integrals of the curvature over large regions of a drop surface are accurate to $O(1/N)$ because line integrals in the interior of the region cancel exactly. Using formula (2.1), integrals of the curvature over half of an axisymmetric surface have a relative error $\approx 5/N$.

2.3. Ewald-summed Stokeslet and stresslet

The kernel functions \mathbf{G} and \mathbf{T} that appear in (2.3) are the Stokeslet and stresslet in a triply periodic lattice. They are evaluated by Ewald-summation on the lattice and reciprocal lattice of image points:

$$G_{ij}(\mathbf{x}) = \sum_l \left[A(\xi|\mathbf{x}^l) \frac{\delta_{ij}}{|\mathbf{x}^l|} + B(\xi|\mathbf{x}^l) \frac{x_i^l x_j^l}{|\mathbf{x}^l|^3} \right] - \frac{8\xi}{\pi^{1/2}} \delta(\mathbf{x}) \delta_{ij} \\ + \frac{8\pi}{L^3} \sum_{\lambda \neq 0} \left[\frac{\delta_{ij}}{|\mathbf{k}^\lambda|^2} - \frac{k_i^\lambda k_j^\lambda}{|\mathbf{k}^\lambda|^4} \right] \left(1 + \frac{|\mathbf{k}^\lambda|^2}{4\xi^2} + \frac{|\mathbf{k}^\lambda|^4}{8\xi^4} \right) e^{-|\mathbf{k}^\lambda|^2/4\xi^2} \cos(\mathbf{k}^\lambda \cdot \mathbf{x}), \quad (2.5a)$$

$$T_{ijk}(\mathbf{x}) = - \sum_l \left[C(\xi|\mathbf{x}^l) \frac{x_i^l x_j^l x_k^l}{|\mathbf{x}^l|^5} + \frac{8\xi^3 |\mathbf{x}^l|^3}{\pi^{1/2}} e^{-\xi^2 |\mathbf{x}^l|^2} \frac{x_i^l \delta_{jk} + x_j^l \delta_{ik} + x_k^l \delta_{ij}}{|\mathbf{x}^l|^3} \right] \\ + \frac{8\pi}{L^3} \sum_{\lambda \neq 0} \left[2 \left(1 + \frac{|\mathbf{k}^\lambda|^2}{4\xi^2} + \frac{|\mathbf{k}^\lambda|^4}{8\xi^4} \right) \frac{k_i^\lambda k_j^\lambda k_k^\lambda}{|\mathbf{k}^\lambda|^4} - \frac{k_i^\lambda \delta_{jk} + k_j^\lambda \delta_{ik} + k_k^\lambda \delta_{ij}}{|\mathbf{k}^\lambda|^2} \right] e^{-|\mathbf{k}^\lambda|^2/4\xi^2} \sin(\mathbf{k}^\lambda \cdot \mathbf{x}), \quad (2.5b)$$

where

$$A(t) = \operatorname{erfc}(t) + \frac{2t}{\pi^{1/2}} (2t^2 - 3) e^{-t^2}; \quad B(t) = \operatorname{erfc}(t) + \frac{2t}{\pi^{1/2}} (1 - 2t^2) e^{-t^2}; \\ C(t) = 6\operatorname{erfc}(t) + \frac{4t}{\pi^{1/2}} (3 + 2t^2 - 4t^4) e^{-t^2}.$$

The stresslet \mathbf{T} is derived from the Stokeslet \mathbf{G} and the latter follows from Beenaker (1986). The volume of each unit cell (normalized by the undeformed drop radius) is L^3 ; ϕL^3 is the dispersed-phase volume in each cell. The lattice points are \mathbf{X}^l and $\mathbf{x}^l = \mathbf{x} - \mathbf{X}^l$; \mathbf{k}^λ are the reciprocal lattice vectors defined such that $\mathbf{X}^\lambda \cdot \mathbf{k}^\lambda$ is an integer (positive or negative) multiple of 2π . As indicated, the zero-wavenumber term is excluded from the reciprocal lattice sum as a general consequence of the mean pressure gradient balancing the mean flow rate, which both vanish in the present problem. The lattice deforms continuously during shear flow but, by its periodicity,

any lattice configuration can be described by configurations corresponding to strains: $-\frac{1}{2} \leq \gamma \leq \frac{1}{2}$; at zero strain, the lattice is simple cubic with spacing L between the image points. The above formulae are independent of the convergence parameter, ξ , which controls the relative convergence rates for the sums over the lattice and reciprocal lattice; when optimally chosen, both sums converge at equal rates. On a cubic lattice, $\xi = \pi^{1/2}/L$ is optimal (Beenaker 1986) and we found extremely rapid convergence using this value for all strains $-\frac{1}{2} \leq \gamma \leq \frac{1}{2}$. With this choice, several decimal place convergence was always obtained by summing over only two layers on the real- and reciprocal-space lattices.

Unfortunately, the Ewald-summed formulae for \mathbf{G} and \mathbf{T} are still far too computationally intensive for large-scale numerical simulations. A much more efficient procedure is to subtract the simple free-space Stokeslet and stresslet

$$\mathbf{G}^0(\mathbf{x}) = \frac{\mathbf{I}}{|\mathbf{x}|} + \frac{\mathbf{x}\mathbf{x}}{|\mathbf{x}|^3}; \quad \mathbf{T}^0(\mathbf{x}) = -6\frac{\mathbf{x}\mathbf{x}\mathbf{x}}{|\mathbf{x}|^5},$$

where \mathbf{x} is the vector to the *nearest* periodic replica, and tabulate the computationally intensive non-singular functions $\mathbf{G} - \mathbf{G}^0$ and $\mathbf{T} - \mathbf{T}^0$ on an evenly spaced rectangular grid in the four-dimensional region: (γ, \mathbf{x}) with $[-\frac{1}{2} \leq \gamma \leq \frac{1}{2}]$ and the three (sheared) spatial coordinates in the interval $[0, \frac{1}{2}L]$ which is sufficient by the symmetries of these functions and the symmetry of the lattice. Since the tabulated functions $\mathbf{G} - \mathbf{G}^0$ and $\mathbf{T} - \mathbf{T}^0$ are smooth, a linear interpolation gives second-order accuracy. The surface integrations in (2.3) were evaluated by adding the interpolated functions to the free-space Stokeslet and stresslet which are trivial to compute. The relative accuracy of \mathbf{G} and \mathbf{T} , computed by this partial tabulation procedure, is further improved because the exactly computed singular functions, \mathbf{G}^0 and \mathbf{T}^0 , dominate the interpolated functions. We obtained better than 1% pointwise convergence using only 8 interpolation points in each spatial coordinate range $[0, \frac{1}{2}L]$ and 16 points for the range of strains $[-\frac{1}{2}, \frac{1}{2}]$. We tested the procedure on a few simulations with only one drop per unit cell and $\phi = 37\%$. The results were obtained by tabulation and by direct evaluation of (2.5) were indistinguishable and in agreement with Pozrikidis (1993); however, the tabulation procedure dramatically reduces the CPU time. In simulations with larger M/ϕ (more drops per unit cell or lower volume fractions), tabulation errors will be smaller because the lattice spacing is larger and drops are therefore less influenced by their images in adjacent cells.

2.4. Numerical solution

For dynamic simulations, (2.3) must be augmented by continuously updating all of the collocation points with the kinematical condition

$$\frac{d\mathbf{x}_0}{dt} = \mathbf{u}(\mathbf{x}_0) + \mathbf{w}(\mathbf{x}_0), \quad (2.6)$$

where $\mathbf{w}(\mathbf{x}_0)$ is defined by (2.2). The stability criterion for time integration is (Rallison 1981)

$$\Delta t \leq K\Delta x \quad (2.7)$$

where K is an order-one constant and Δx is the *minimum* separation between the collocation points on any given drop interface which is $O(1/N^{1/2})$ for a fairly uniform grid; separation between collocation points on *different* drop surfaces does not affect stability but the step size must be sufficiently small to avoid surface overlap. In agreement with Rallison (1981), we found $K = \frac{1}{2}$ approximately optimal: our

numerical results were insensitive to smaller values and $K = 1$ was unstable. A second-order Runge–Kutta scheme was used to integrate (2.6), thereby introducing a $\Delta t^2 = O(1/N)$ time integration error, consistent with the errors resulting from the surface integration in (2.3). There is no apparent need to use higher-order time integration.

At each time step, (2.3) was solved iteratively by inserting velocities from one iteration into the right-hand side of the equation. Velocities computed at the previous time step were used as the initial guess. Depending on the viscosity ratio, only a few iterations were required for convergence to 10^{-4} pointwise relative error; the results were unaffected by smaller tolerances. For the first time step, $\mathbf{u}(\mathbf{x}_0) = 0$ was used for the initial guess and more iterations were required to solve (2.3). For $\lambda < 1$, somewhat faster convergence was obtained by combining the second term on the right-hand side of (2.3) with the left-hand side. This procedure results in computation times that scale as $O(N \times M)^2$ per time step; matrix inversion is an unattractive alternative that increases this estimate to $O(N \times M)^3$. Equation (2.3) has eigensolutions that cause unphysical changes in the dispersed-phase volume at small viscosity ratios, corrupt numerical solutions at large viscosity ratios, and slow the iterative convergence. These detrimental effects were eliminated by implementing Wielandt eigenvalue deflation (Pozrikidis 1992, pp. 120–127) to purge the solution of these eigenfunctions.

The bulk stress of an emulsion in shear flow can be expressed as the stress that would result from only the continuous-phase fluid and the extra stress that results from the dispersed-phase drops (Batchelor 1970):

$$\Sigma_{ij} = \frac{1}{L^3} \sum_{j=1}^M \int_{S_j(\mathbf{x})} [\kappa(\mathbf{x})n_i x_j + (\lambda - 1)(u_i n_j + n_i u_j)] d\mathbf{x} \quad (2.8)$$

where surfactant-induced Marangoni stresses are neglected, neutral buoyancy is assumed, and the result is normalized by σ/a . To include the effect of a short-range potential interaction (or drops with differing surface tensions), $\kappa(\mathbf{x})$ must be replaced by $f(\mathbf{x})$, defined by (2.4) (with $Bo = 0$). The continuous-phase fluid contributes only to the total shear stress, $Ca + \phi \Sigma_{12}$; normal stress differences result entirely from the dispersed-phase contribution: ϕN_1 and ϕN_2 , where $N_1 = \Sigma_{11} - \Sigma_{22}$ and $N_2 = \Sigma_{22} - \Sigma_{33}$. By symmetry, the time average of $\Sigma_{13} = \Sigma_{23} = 0$ must vanish.

The significance of (2.8) is effectively illustrated by considering the stress contribution of the simple capsule-shaped drop defined in figure 2. For $\lambda = 1$, the above formula yields

$$\Sigma_{12} = \frac{3}{4}ab \sin 2\alpha, \quad N_1 = \frac{3}{2}ab \cos 2\alpha; \quad ab = \frac{2D}{\left[1 - \frac{1}{4}D^2(3 + D)\right]^{1/3}}, \quad (2.9)$$

where the capsule dimensions a and b , or equivalently, the Taylor deformation and orientation, D and α , defined in figure 2, are assumed to be known microstructural parameters. Herein, these formulae are only used for crudely predicting the shear and normal stress contributions from the average shape and orientation obtained from the simulations. Because of its axisymmetry, the capsule shape does not predict the smaller, second normal stress difference. These simple formulae are inaccurate at larger capillary numbers, close to drop breakup, and they do not describe the effect of the dispersed-phase viscosity. Fortunately, however, the above expressions are accurate within a few percent under dilute conditions for $\lambda = 1$ and $Ca \leq 0.3$.

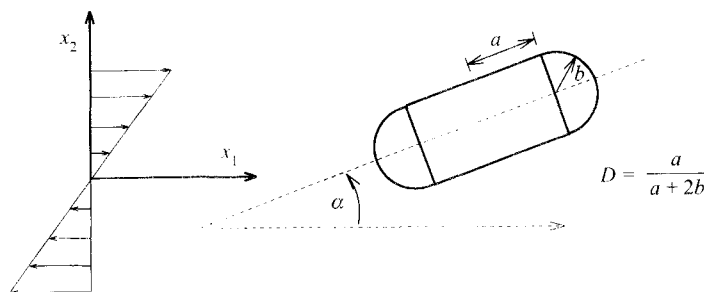


FIGURE 2. Capsule-shaped drop in shear flow constructed from a circular cylinder with hemispherical caps. Sketch defines flow geometry and Taylor deformation, D , and orientation, α , for a drop.

2.5. Computation speed

The computational procedure, described above, successfully computes steady-state rheological behaviour with modest CPU time on a work station. The computation time is dominated by the $O(M \times N)^2$ integrand evaluations needed for the surface integrals in (2.3) at each time step, where M is the number of drops used in the simulation and N is the number of triangular boundary elements on each drop surface; for time steps given by (2.7), the overall CPU time is $O(M^2 \times N^{5/2})$. As an example, numerical simulations for $\phi = 30\%$, $Ca = 0.3$, and $\lambda = 1$ using 12 drops per unit cell and 320 boundary elements per drop (figures 5 and 6), proceeded at the rate of 17 seconds per time step ($\simeq 0.01$ strain) on a Hewlett-Packard 9000 series 735 workstation with a standard optimizing FORTRAN compiler. The table of values for the Stokeslet and stresslet interpolation procedure is computed and stored once at the beginning of each simulation; this requires a trivial amount of memory (65 kbytes) and negligible CPU time, equal to about one time step. According to the results depicted in figure 6, steady-state results for this case are achieved with strains of 10. Steady-state results therefore require less than five hours of workstation computing time. In fact, the results depicted in figure 7 indicate that steady-state results may even be obtained in only one hour on a workstation: computation times are proportional to M^2 and, under some conditions, very nearly the same results were obtained using only 6 drops per unit cell. For $\lambda = 1$, (2.3) provides the fluid velocity at collocation points explicitly; a more time-consuming iterative solution of (2.3) is required for $\lambda \neq 1$, as described in §2.4. For modest viscosity ratios, $\lambda = \frac{1}{2}$ or 2, computation times were about twice as long; for more extreme values, $\lambda = \frac{1}{10}$ or 5, CPU times were approximately four times longer than for the case of equal dispersed- and continuous-phase viscosities.

3. Numerical results

3.1. Test results

To successfully simulate the flow of a concentrated emulsion, the calculation procedure must be able to describe the interaction of two closely interacting drops as depicted in figure 3. Figure 3(a,b) demonstrates that interactions between deformable drops tend to increase the cross-flow separation of their centres. According to figure 3(a,c,d), the deformation and shear stress contribution of the drops are maximal when the drops are pressed together along the compressional axis of the shear flow and minimal when they are drawn apart along the extensional axis. Normal stress

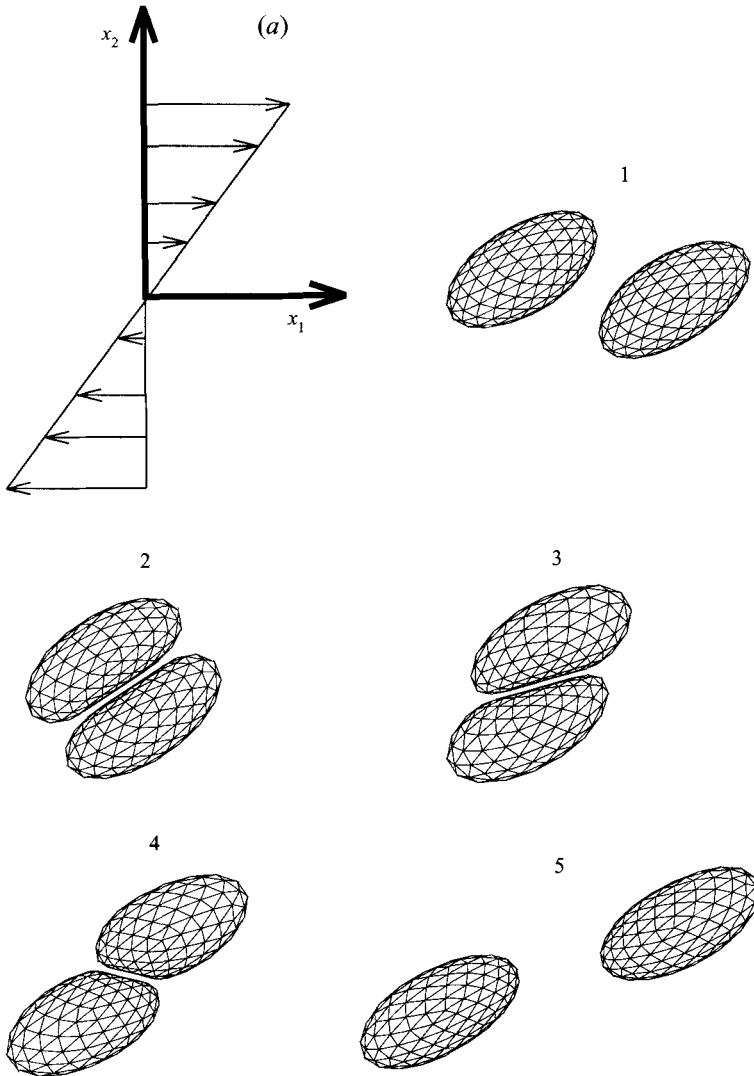


FIGURE 3. (a) For caption see facing page.

contributions are maximal when the drops are more aligned with the flow. These observations demonstrate the connection between the stress contribution of the drops and their geometry (shape and orientation), as implied by (2.8) and illustrated by formulae (2.9).

The results depicted in figure 3(a,b) are consistent with the fact that deformation drastically reduces drop coalescence rates. Asymptotic calculations for $Ca \ll 1$ indicate that, in the absence of van der Waals attraction, drop deformation prevents drop coalescence (Yiantsios & Davis 1991); there are no previous studies for $Ca = O(1)$. Figure 3(a) illustrates that uniform collocation grids are maintained on the drop surfaces with a higher density of collocation points in the near-contact region and on highly curved regions; this is a direct consequence of the tangential redistribution velocity, defined by equation (2.2), and it is essential for successfully simulating concentrated emulsion flow.

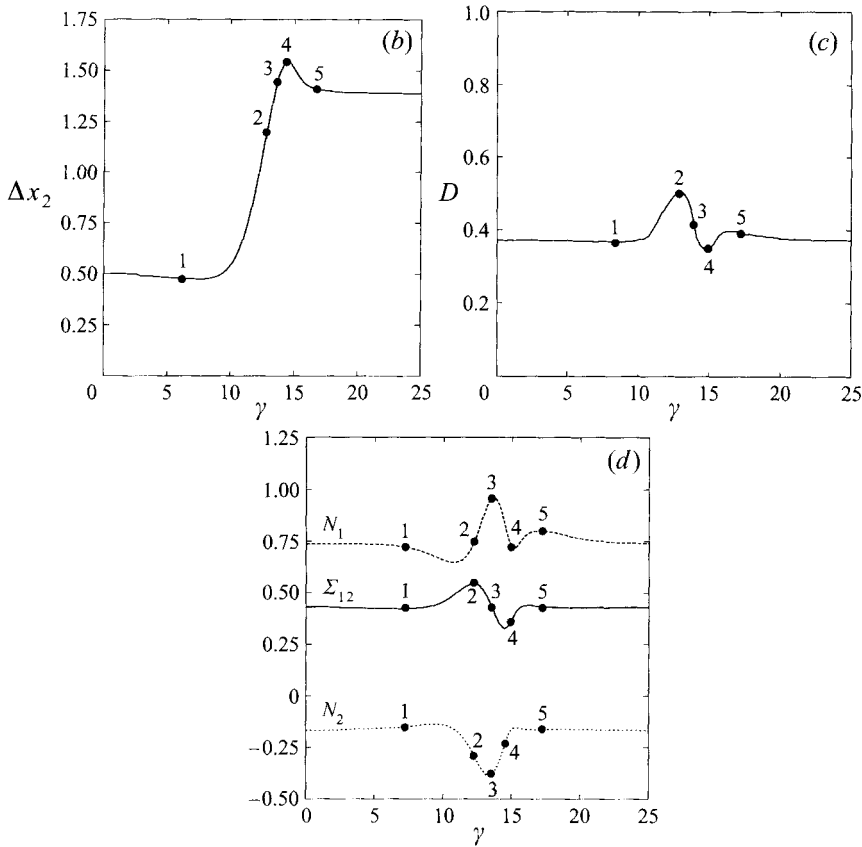


FIGURE 3. Sequence of two closely interacting equal drops in an unbounded shear flow; $Ca = 0.3$, $\lambda = 1$; 320 triangles are used to discretize each drop surface. (a) Collocation grids at four successive instants during the interaction and quantitative results as a function of strain: (b) cross-flow separation of drop centres in the x_2 -direction; (c) drop deformation; (d) stress contribution of each drop to shear stress (solid curve), first normal stress difference (dashed curve), second normal stress difference (dotted curve). The numbered \bullet points in (b), (c), and (d) correspond to the numbered sequence illustrated in (a).

As a test of our three-dimensional boundary integral calculations, we performed the axisymmetric calculation for the super-critical capillary number conditions depicted in figure 4. We compared our results to those obtained by M. Manga (personal communication) using an intrinsically more accurate axisymmetric formulation. At modest deformations, our three-dimensional calculations accurately predict the drop shape using 320 boundary elements. However, at larger deformations, our calculations with the same number of collocation points considerably over-predict drop deformation. The error is substantially, but not entirely, reduced by increasing the number of boundary elements to 720. Apparently, locally inaccurate curvatures effectively cancel for modest, but not large, drop deformations. The singularity subtracted integrand of (2.3) is a non-singular but rapidly varying function in highly curved regions because of its dependence on the local orientation of the surface; the integral therefore becomes more sensitive to pointwise curvature values. Equation (2.1) tends to smooth out curvature values by its dependence on the adjacent collocation points: curvatures and the corresponding capillary pressures they induce are too low

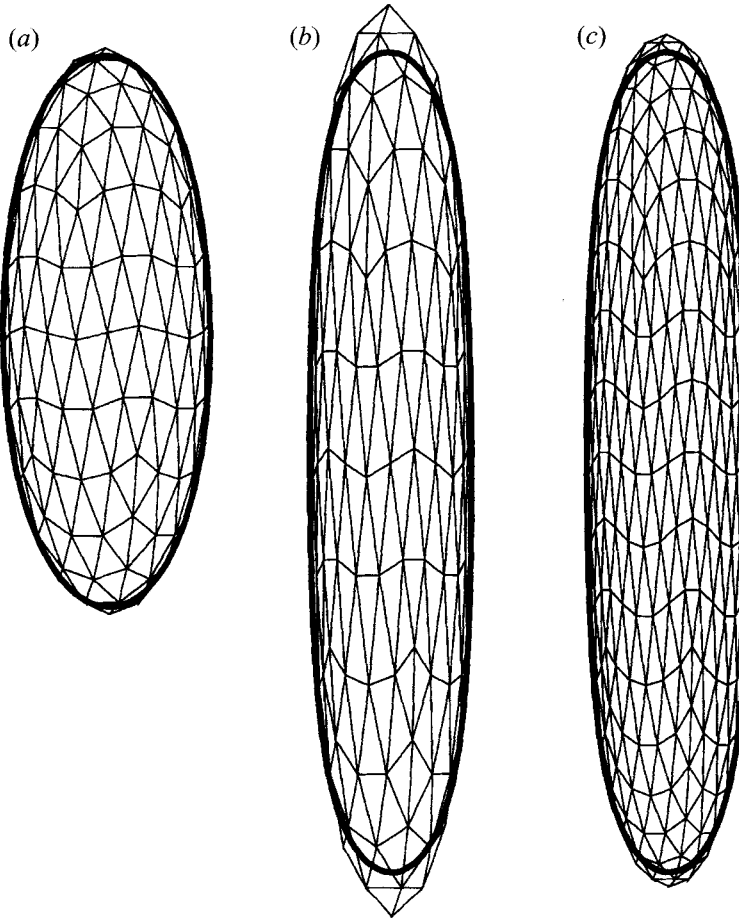


FIGURE 4. Isolated drop in uniaxial extension; $Ca = 0.2$, $\lambda = 1$; (a) strain= 1, (b,c) strain= 2. Solid curves were obtained by axisymmetric calculations of M. Manga (personal communication); collocation grid depicts results using 320 triangles (a,b) and 720 triangles (c) on the drop surface.

in highly convex regions. As a result, viscous stresses are undercompensated and the resulting deformation is too large. The highly elongated boundary elements visible in figure 4(b,c), illustrate the shortcoming of a triangulation with static connections at high deformations. Fortunately, the drop deformations observed in our simulations of concentrated emulsions were smaller than that shown in figure 4(b,c).

We also tested our calculations against the calculations of Kennedy *et al.* (1994) for an isolated drop in a shear flow at several viscosity ratios. In most cases, the results agreed to within the accuracy of reading results from the published figures. The only minor discrepancies occurred for large deformations; our results predict drop breakup (absence of a stationary shape) at slightly higher capillary numbers than those reported by Kennedy *et al.* (1994). As explained above, our curvature calculation procedure systematically yields erroneously *large* deformations and therefore erroneously *low* critical capillary numbers; we expect that the actual critical capillary numbers should *exceed* our values. We found very close agreement to the results of Pozrikidis (1993) for a regular lattice of drops (one drop per unit cell) with $\lambda = 1$, which provided a useful test of our overall procedure for incorporating

periodic boundary conditions by partial tabulation of the Ewald-summed Stokeslet and stresslet. Our results are consistent with the semi-dilute theory of Zinchenko (1984) for $Ca = 0$, as figure 11 illustrates, but a quantitative comparison was not possible.

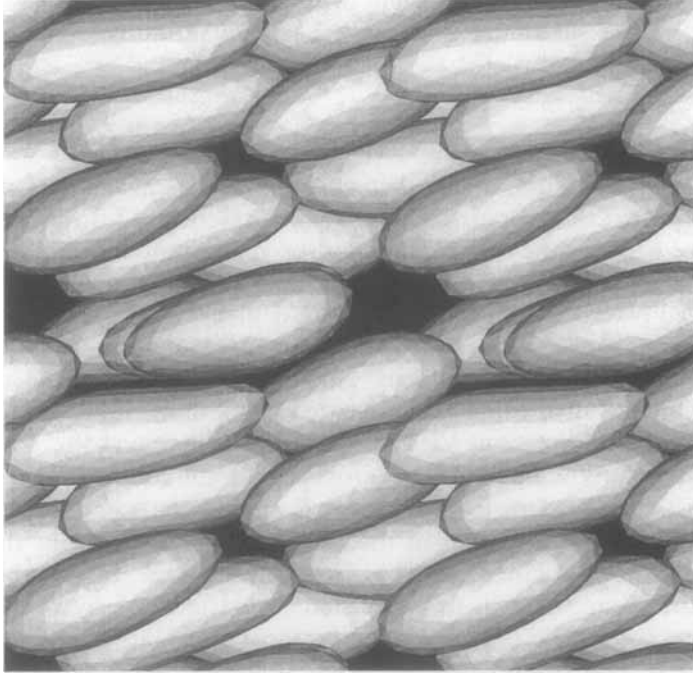
3.2. Transient, concentrated emulsion in shear flow

Figure 5 shows the microstructure predicted by our numerical simulation for a concentrated emulsion with 30% dispersed-phase volume fraction; 12 drops were used in the unit cell. Figure 6 shows the corresponding drop deformation, orientation, and stress contributions. Results are depicted for each of the 12 drops in a unit cell (thin curves); volume-averaged (over the unit cell) results are depicted by the thick curves. Figure 5 clearly shows an anisotropic microstructure of drops that forms after a strain of 10. Viewed in the vorticity (5a) or velocity gradient direction (5c), the microstructure reveals closely spaced drops that are elongated in the flow direction and, to a lesser extent, in the vorticity direction. Viewed in the flow direction (5b), however, the microstructure is much more open and the cross-section for collisions thereby reduced.

Under the conditions depicted in figures 5 and 6, the total shear stress in the emulsion is only 35% larger than in the continuous-phase fluid at the same shear rate and the first normal stress is 85% of the shear stress. In the absence of drop deformation, the shear stress in this emulsion would increase by over 80% and the first normal stress would be only 2–3% of the shear stress, according to the theory of Zinchenko (1984). This example demonstrates that drop deformation and alignment with the flow dramatically lowers the shear stress and produces very large elastic stresses. The microstructure shown in figure 5 helps to explain why emulsions are so strongly shear thinning and have such large normal stresses: the reduced collision cross-section of the drops (figure 5b) allows them to glide past each other with less resistance and the elongation of the drops in the flow direction produces large first normal stress differences. Given the microstructure illustrated in figure 5, these qualitative features are consistent with stress contributions of the drops given by formulae (2.9).

According to the heavy curves in figure 6, steady-state rheological behaviour and microstructure are attained with strains of 10. This assertion is confirmed by the large-strain simulations, γ up to 30, depicted in figure 7. Small fluctuations in the volume-averaged quantities are a consequence of the finite number of drops used in the simulations. By contrast, the instantaneous contributions from the *individual* drops shown by the lighter curves in figure 6, fluctuate strongly about the mean value, without apparent decay. The time-averaged off-diagonal stresses, Σ_{13} and Σ_{23} are very close to zero as required by symmetry but the contributions from individual drops exhibit fluctuations as large as the fluctuations for the other stress components. The fluctuations exhibited by individual drops may be qualitatively understood from the pair interaction depicted in figure 3 for isolated drops under the same flow conditions. Interactions between drops in a concentrated emulsion cause fluctuations in their shape and orientation that induce fluctuations in their stress contributions, as implied by (2.9). A comparison of the results shown in figures 3 and 6 indicates that fluctuation for drops in a concentrated emulsion are considerably larger than for dilute emulsions, probably because drops are forced to squeeze closely past each other in dense systems. Animated sequences from our numerical simulations show that the anisotropic microstructure depicted in figure 5 forms as the emulsion flows because interactions between the drops tend to increase their cross-flow sepa-

(a)



(b)

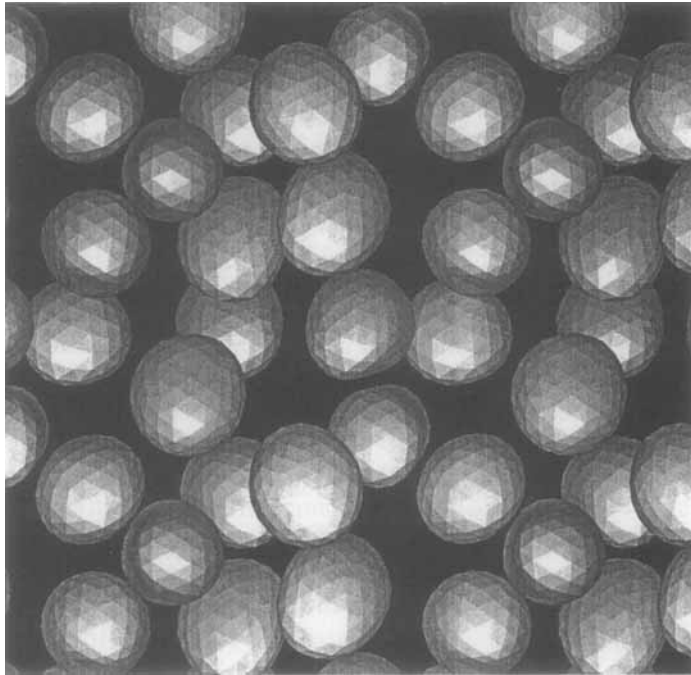


FIGURE 5. (a,b) For caption see facing page.

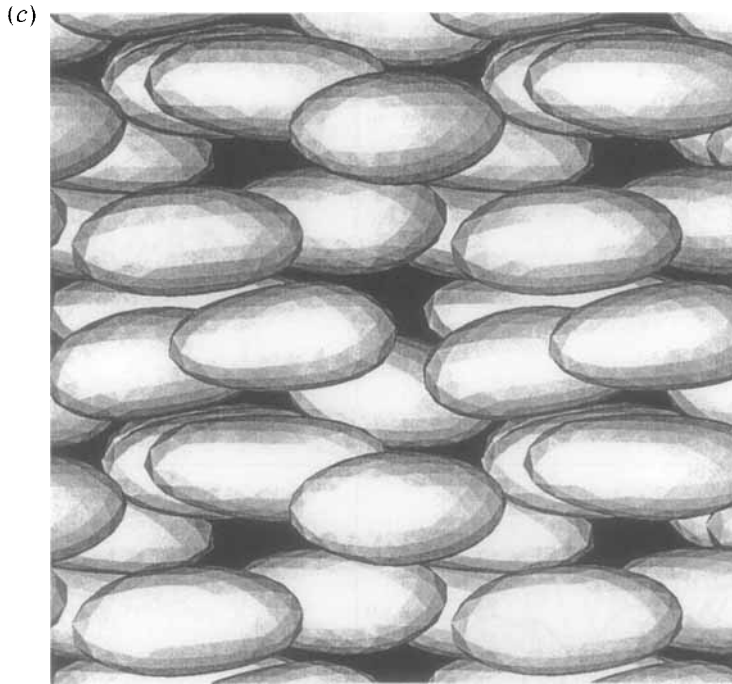


FIGURE 5. An emulsion in shear-flow after strain = 10: numerical simulation using 12 equal drops (1.5 unit cells are shown) with 320 triangles on each drop surface; $\phi = 30\%$, $Ca = 0.3$, $\lambda = 1$; initially the drops are undeformed and randomly located. (a) View in the vorticity direction (x_3 -direction), (b) view in the flow direction (x_1 -direction), (c) view in the direction of velocity gradient (x_2 -direction).

ration and alignment in the flow direction, qualitatively like the sequence depicted in figure 3.

Most of the results presented in this article were obtained from simulations with 12 drops per unit cell and the results were compared to those obtained from simulations with fewer drops to verify convergence with respect to the number of drops used. The volume-averaged results depicted in figure 7 show very similar results obtained from three simulations with 12 drops per unit cell (thick curves) and three simulations with only 6 drops per unit cell (thin curves). A limited number of simulations using an intermediate number of drops and with slight polydispersity gave very similar results, eliminating the possibility of apparent convergence resulting from an artifact of symmetry. However, numerical simulations with fewer than 4 drops per unit cell erroneously predicted drop breakup under the same conditions, demonstrated by drop deformation that increases monotonically without attaining a stationary value; this result appears to be an artifact of drops interacting closely with their images in adjacent unit cells when the unit cell dimension, $L = (N/\phi)^{1/3}$, is decreased. By contrast, simulations of concentrated rigid-particle suspensions often require a very large number of particles for reliable rheological predictions, primarily because of particle clustering during flow (Brady & Bossis 1988). Apparently, drop deformation suppresses strong correlations that result from cluster formation: geometrical blockages of rigid particles are eliminated by even small deformations of the emulsion droplets.

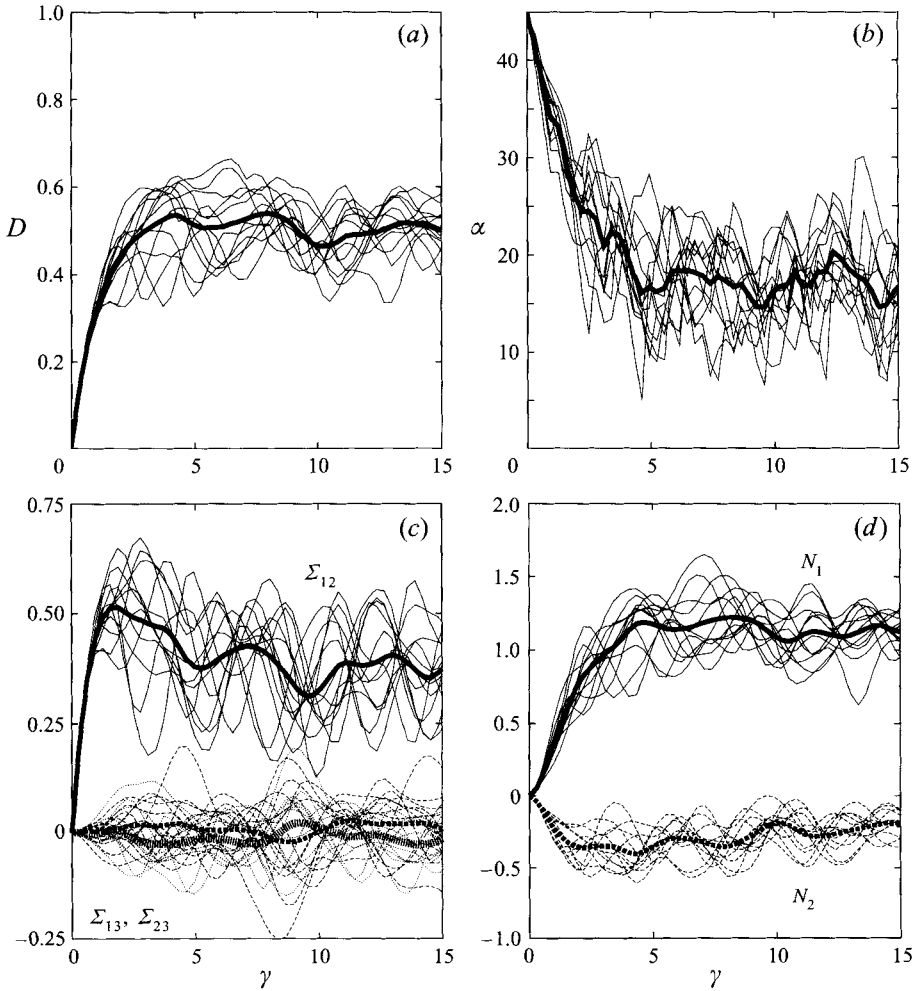


FIGURE 6. Results as a function of strain obtained by the simulation described in figure 5 caption: (a) drop deformation D , (b) orientation α , and (c,d) stress contributions of each drop: shear stress, Σ_{12} (c, solid curves), first normal stress difference, N_1 (d, solid curves), second normal stress difference, N_2 (d, dashed curves), and asymmetric off-diagonal stress components Σ_{13} (c, dashed curves), Σ_{23} (c, dotted curves). Thin curves depict results for individual drops, thick curves are average values for the 12 drops.

The starting conditions used for our simulations correspond to zero flow and disordered microstructure: initially, non-overlapping spherical drops were placed at random into the unit cell. Each of the simulations depicted in figure 7 began with a distinct, disordered microstructure generated in this way. By comparing simulations with the same number of drops, we confirm, from figure 7, that the time-averaged rheological and microstructural results are insensitive to their initial, random configuration.

Convergence of the numerical simulation with respect to the surface discretization is demonstrated by the results depicted in figure 8 from four simulations using $N = 180, 320, 500,$ and 720 triangular boundary elements on each drop surface (thicker curves correspond to increased N). Extremely crude results are obtained with $N = 180$. Elsewhere in this article, the results were obtained using $N = 320$; comparing the

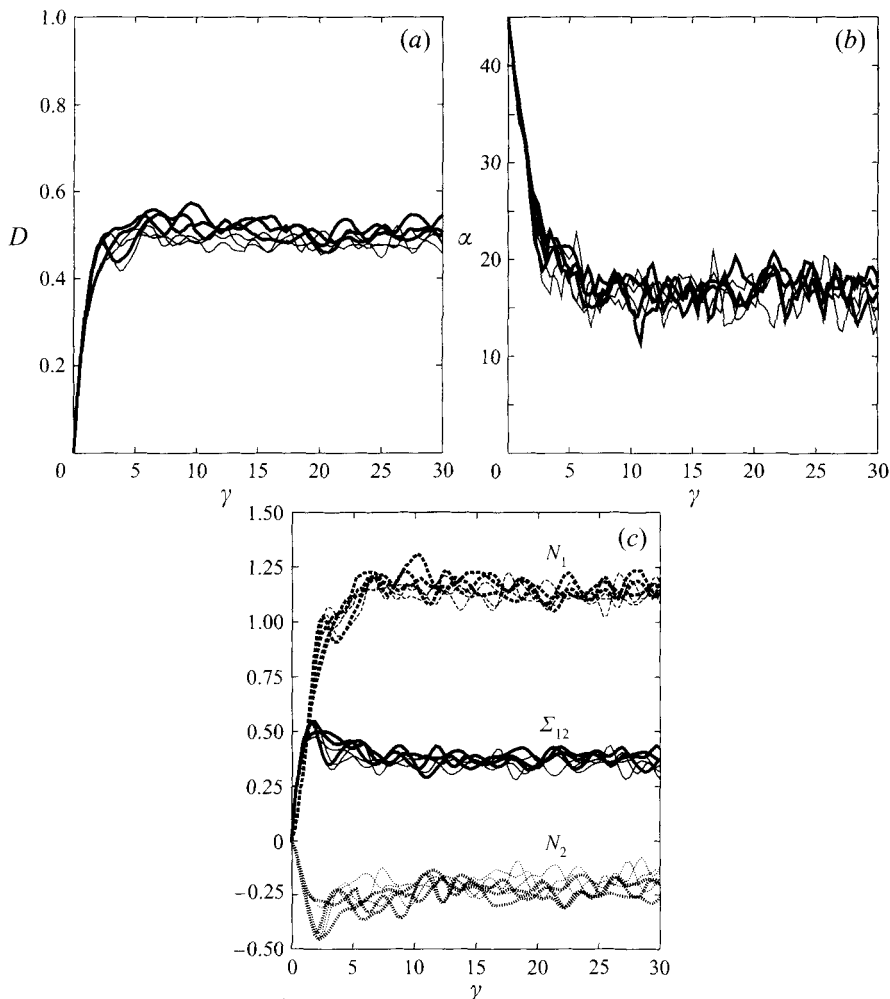


FIGURE 7. Effect of initial configuration and the number of drops used in simulation; volume-averaged results as a function of strain from six simulations with $\phi = 30\%$, $Ca = 0.3$, $\lambda = 1$; each simulation used a different random initial configuration of drops. Thick curves depict results from three simulations with 12 drops (320 triangles on each drop surface); thin curves depict results from three simulations with 6 drops. (a) Average drop deformation and (b) orientation, and (c) average stress contributions of drops: shear stress (solid curves), first normal stress difference (dashed curves), and second normal stress difference (dotted curves).

results shown in figure 8, we conclude that our results are accurate to about 5%. The slow convergence shown by the results depicted in figure 8, particularly for large N , probably reflects the inherently inaccurate curvature calculation. As explained in the previous subsection, curvature errors lead to excessive drop deformation. As a consequence, and by a similar relative error, the orientation angle of the drops, α , is too low: the drops orient excessively into the flow direction. The simplified expressions (2.9) for the stress contributions of the drops indicate that these errors lead to first normal stress differences that are too large by roughly twice the relative error in drop deformation (noting that $\alpha < 45^\circ$ always); fortunately, these errors tend to cancel for the shear stress contribution of the drops. Figure 8 appears to be

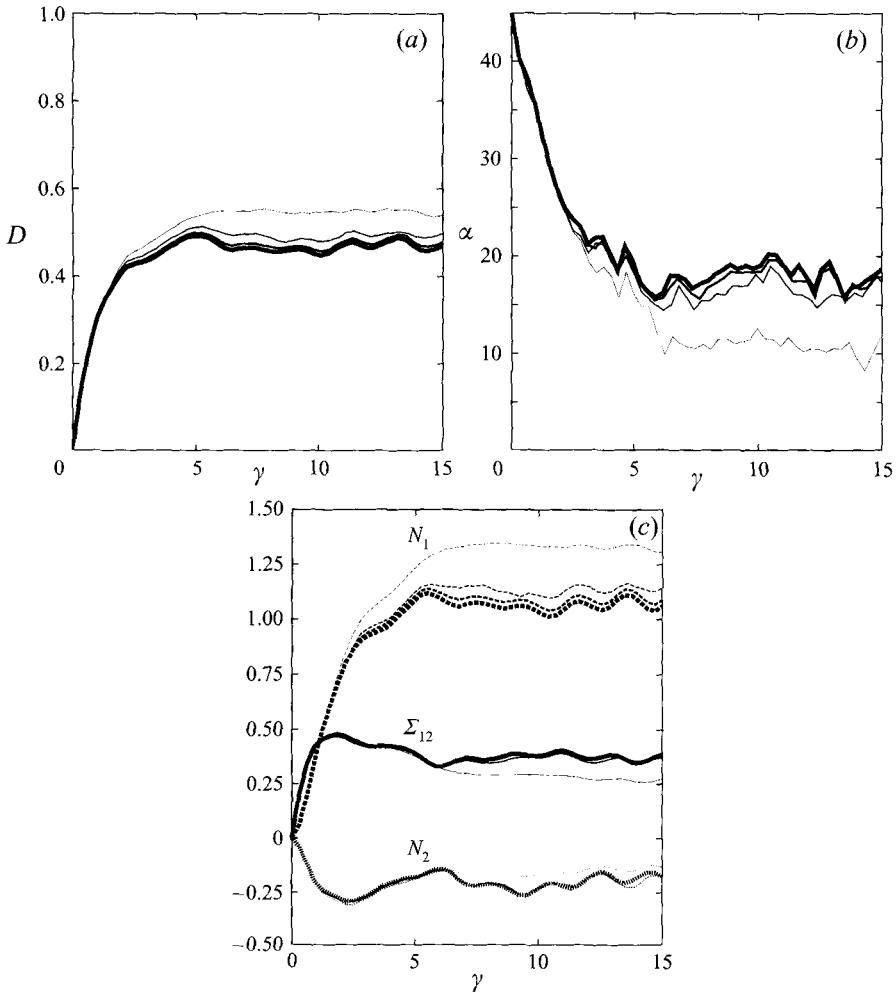


FIGURE 8. Effect of surface discretization. Results as a function of strain from three simulations with $\phi = 30\%$, $Ca = 0.3$, $\lambda = 1$; each simulation used the same random initial configuration of 6 drops. Four sets of curves depict results obtained using 180, 320, 500, and 720 triangles on each drop surface; faintest curves correspond to 180 triangles per drop and thickest correspond to 720. (a) Average drop deformation and (b) orientation, and (c) average stress contributions of drops: shear stress (solid curves), first normal stress difference (dashed curves), second normal stress difference (dotted curves).

consistent with this heuristic argument. The second normal stress difference is also more accurately obtained because it depends on deformation in the vorticity direction which is modest (figure 5b) and therefore more accurately described, as the results in figure 4 demonstrate.

Figure 9 illustrates the effect of an *ad hoc* short-range repulsive force acting between the drops. The repulsive force used for these results was described by (2.4) with $H = 0.1$,

$$g(h) = \frac{1}{h_0} \frac{e^{-h/h_0}}{1 - e^{-h/h_0}},$$

where $h_0 = 0.1$ is the dimensionless interaction range. The results indicate that the repulsive force has negligible effect on the rheology of the emulsion; the effect on

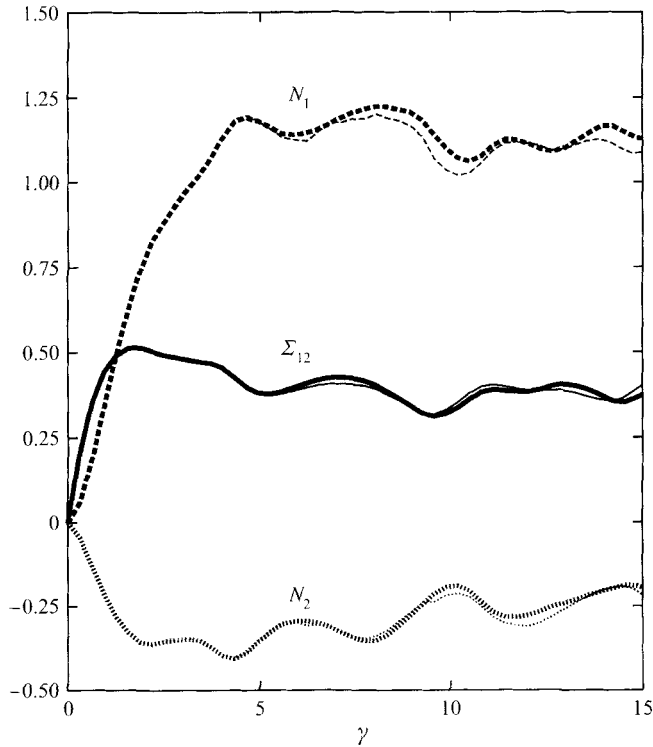


FIGURE 9. Effect of short-range repulsion. Average stress contributions of the drops as a function of strain from two simulations with $\phi = 30\%$, $Ca = 0.3$, and $\lambda = 1$; each simulation used the same initial configuration of 12 drops with 320 triangles on each drop surface. Thin curves depict results obtained from a simulation with short-range repulsion between the drop surfaces, thick curves were obtained without repulsion; shear stress (solid curves), first normal stress difference (dashed curves), second normal stress difference (dotted curves).

the microstructure was similarly negligible. Under low-capillary-number conditions ($Ca < 0.15$), larger strains could be obtained only with a repulsive interaction but otherwise it had little effect on the results. At zero capillary number, drop coalescence can occur without van der Waals attraction (Zinchenko 1983); thus, the semi-dilute theory of Zinchenko (1984) invokes an infinitely short-range repulsive interaction between the drops.

4. Steady-state results

As discussed in §3, the steady-state rheology and microstructure is attained after strains of about 10. The steady-state results depicted in figures 10 and 11 were obtained by time averaging the results of transient calculations, such as those illustrated in figure 7, over a time interval long compared to transient fluctuations after steady-state behaviour was attained (e.g. $\gamma > 10$). Each symbol on the curves shown in figures 10 and 11 represents a large strain, numerical simulation.

4.1. Effect of dispersed-phase volume fraction

The results depicted in figure 10(a,b) show that drops deform more and orient more into the flow direction as the dispersed-phase volume fraction is increased. A comparison of the dilute, pairwise interaction depicted in figure 3(a) and the

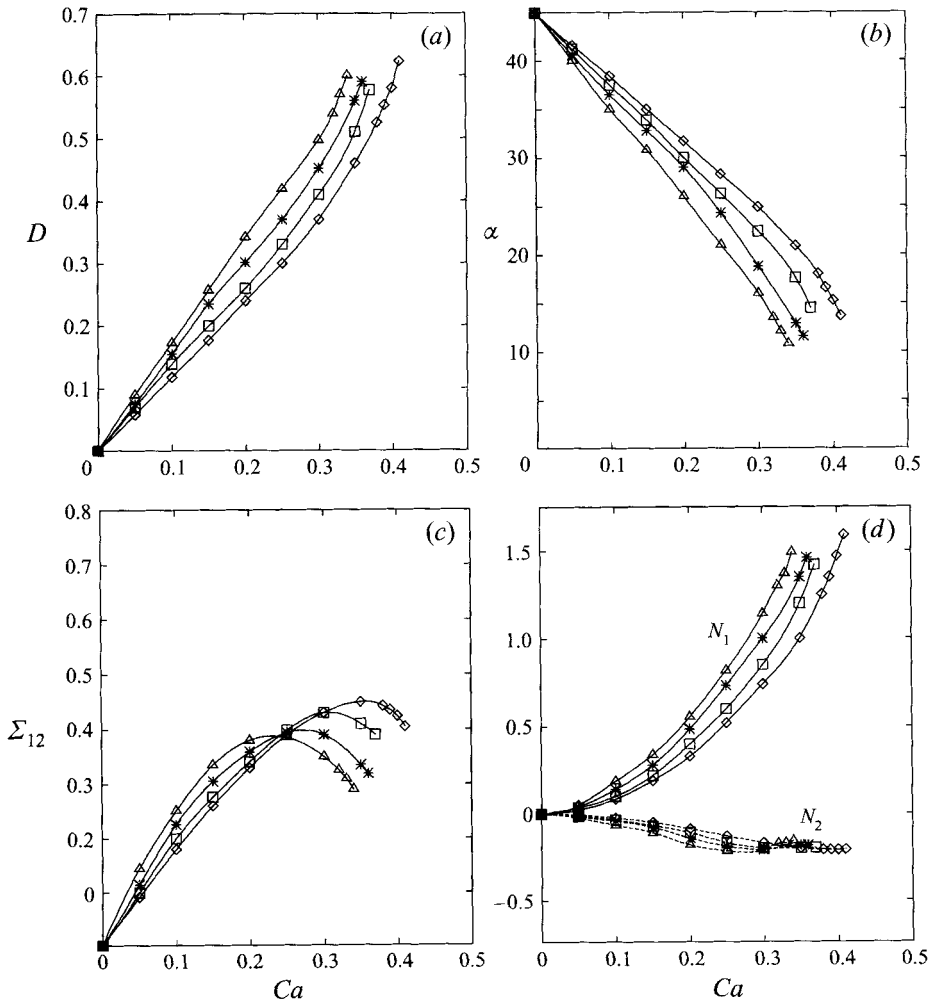


FIGURE 10. Steady-state results as a function of capillary number for $\lambda = 1$. (a) Average steady-state drop deformation, (b) drop orientation, (c) shear stress contribution of drops, and (d) contribution of drops to normal stresses: first normal stress difference (solid curves), second normal stress difference (dashed curves); $\phi = 0$ (\diamond), $\phi = 10\%$ (\square), $\phi = 20\%$ (*), $\phi = 30\%$ (\triangle).

concentrated flow illustrated in figure 5(a) illustrates this trend. At the terminal point of the upwardly concave drop deformation curves, shown in figure 10(a), drop breakup seems imminent; average drop deformation increased monotonically without attaining a stationary value at larger capillary numbers. The results indicate that drop breakup occurs at slightly lower capillary numbers in more concentrated emulsions.

Figure 10(d) indicates that the first normal stress difference increases rapidly with shear rate and with increasing dispersed-phase volume fraction. At a dispersed-phase volume fraction of 30%, the total first normal stress difference, ϕN_1 , is nearly equal to the total shear stress in the emulsion, $Ca + \phi \Sigma_{12}$. The latter is a direct consequence of the increased drop deformation and alignment that occurs at higher volume fractions, according to the simplified formulae (2.9) for the stress contribution of the drops. Similarly, the slight flattening of the drops in the vorticity direction, seen

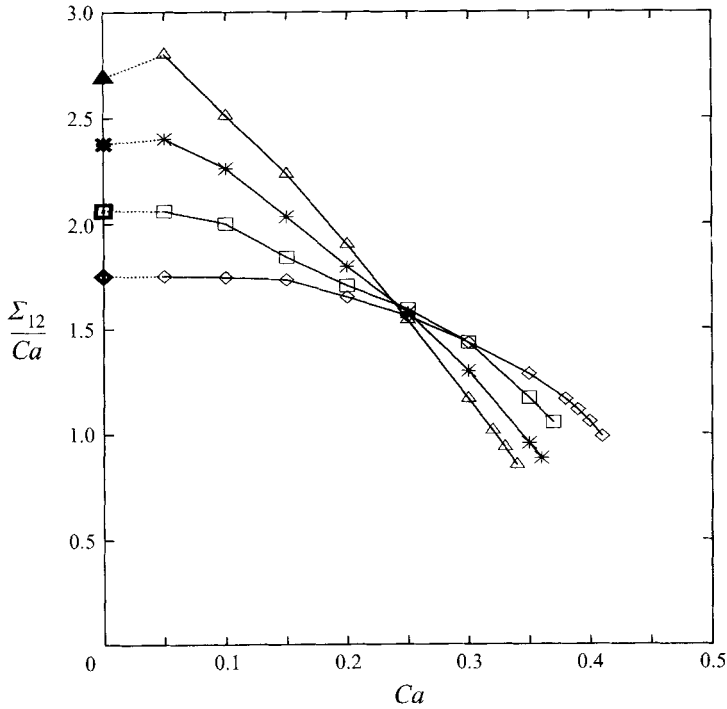


FIGURE 11. Steady-state effective shear viscosity contribution of drops, Σ_{12}/Ca , as a function of capillary number for $\lambda = 1$; $\phi = 0$ (\diamond), $\phi = 10\%$ (\square), $\phi = 20\%$ ($*$), $\phi = 30\%$ (\triangle). Bold symbols denote values for $Ca = 0$ obtained from semi-dilute theory (Zinchenko 1984)

in figure 5(b), is consistent with the small negative second normal stress differences shown in figure 10(d).

According to figure 10(c), the shear stress contribution of the drops is insensitive to the dispersed-phase volume fraction; thus, the shear stress is roughly linear in the dispersed-phase volume fraction. This result contrasts with the sharply increasing shear viscosity in suspensions of rigid particles or spherical drops with increasing volume fraction. This is a consequence of the drop deformation, as the discussion in the second paragraph of §3.2 indicates. Figure 10(c) shows strongly shear-thinning behaviour, particularly at larger volume fractions. However, the total shear stress is a monotonically increasing function of shear rate. Figure 11 shows the effective shear viscosity contribution of the drops, Σ_{12}/Ca . The values for $Ca = 0$, corresponding to spherical drops, were obtained from the theory of Zinchenko (1984) that is accurate to $O(\phi^2)$. The results show that shear thinning increases considerably with the dispersed-phase volume fraction. For $Ca = 0$, the effective viscosity contribution of the drops increases by over 50% as the volume fraction is increased to 0.3. The shear viscosity contribution of the drops increases with volume fraction at lower shear rates because of drop collisions; at $Ca = 0.25$, the viscosity contribution of the drops is nearly independent of volume fraction. Shear thinning, which results from drop deformation, is enhanced by drop interactions, thus the shear viscosity contribution of the drops *decreases* with volume fraction at higher shear rates.

Zinchenko's (1984) semi-dilute theory for $Ca = 0$ also predicts small $O(\phi^2)$ normal stresses that are both negative. The values that he reports are much smaller than the

$O(\phi)$ normal stresses predicted for a dilute emulsion of deformable drops (Kennedy *et al.* 1994). For modest capillary numbers, our results predict normal stresses that are an order of magnitude larger than the results for moderately concentrated emulsions with spherical drops. The discussion in the second paragraph of §3.2 exemplifies this point. The discrepancy between Zinchenko's (1984) semi-dilute zero-capillary-number theory and our results in the limit $Ca \rightarrow 0$ can be attributed to the neglected $O(\phi^3)$ (positive) contribution in the dilute theory and the fact that our numerical calculations are less accurate at very small capillary numbers.

4.2. Effect of dispersed-phase viscosity

The results depicted in figure 10 indicate that qualitatively similar rheology and microstructure is predicted for all volume fractions in the range $0 \leq \phi \leq 30\%$. Because of this somewhat unexpected result, we can usefully examine the effect of the dispersed-phase viscosity at a fixed dispersed-phase volume fraction. Figure 12 shows the results from numerical simulations with viscosity ratios in the range $0 \leq \lambda \leq 5$ and the dispersed-phase volume fraction fixed at 10%.

Our simulations predict qualitatively similar behaviour for $\lambda \leq 2$. The results depicted in figure 12(a,b) show a slight trend towards greater deformation and orientation with increasing λ , although the results for $\lambda = 1$ and $\lambda = 2$ are almost indistinguishable. However, the shear-thinning behaviour is a strong function of the viscosity ratio. The first normal stress difference is a very weak function of viscosity ratio for $\lambda \leq 2$ but the results show that the second normal stress difference is considerably larger for viscosity ratios smaller than unity. According to slender-body theory (Hinch & Acrivos 1980), low-viscosity drops become very highly extended before breakup; for $\lambda = 0$ breakup is theoretically impossible for an isolated drop in steady shear flow; however, the effect of transient drop interactions is unknown. The numerical results depicted in figure 12(a) suggest that larger deformations are obtained for smaller viscosity ratios but we are unable to quantitatively resolve the question of low-viscosity drop breakup in concentrated emulsions.

Qualitatively distinct behaviour is observed for $\lambda = 5$. Drop deformation and orientation and contributions to the stress tend to stationary asymptotic values at large shear rates. Non-shear-thinning Newtonian rheological behaviour is predicted at high shear rates. No breakup is predicted for this case, consistent with observations (Grace 1982) and numerical results (Kennedy *et al.* 1994) for an isolated drop with $\lambda \geq 4$ in steady shear flow. For a sufficiently viscous drop, the characteristic time for drop deformation, $(1 + \lambda)\mu a/\sigma$, exceeds the characteristic time for drop rotation, $1/\dot{\gamma}$; hence, the drop rotates from the extensional to the compressional quadrant of the velocity gradient before being significantly deformed, and this prevents breakup. Apparently, unsteady drop interactions and mutually hindered drop rotation are insufficient to induce breakup of more viscous drops at moderate disperse-phase volume fractions.

We obtained qualitatively similar results from numerical simulations with other dispersed-phase volume fractions. Compared to the results shown in figure 12, the results from simulations with larger volume fractions, up to 30%, indicate that drop deformation and orientation have the same trend with respect to λ but it is more pronounced. Unfortunately, we were unable to obtain results for $\lambda = 0$ or $\lambda = 5$ at 30% volume fraction owing to numerical difficulties.

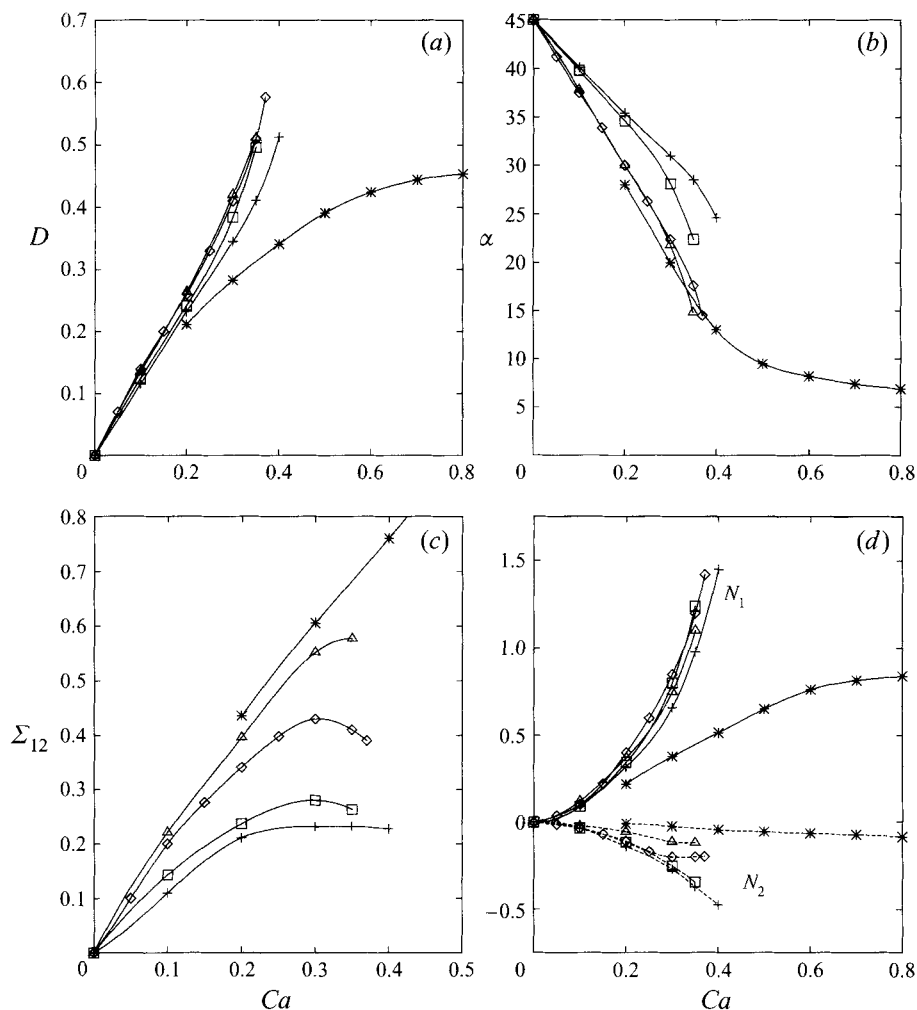


FIGURE 12. Steady-state results as a function of capillary number for $\phi = 10\%$; (a) average steady-state drop deformation, (b) drop orientation, (c) shear stress contribution of drops, and (d) contribution of drops to normal stresses: first normal stress difference (solid curves), second normal stress difference (dashed curves); $\lambda = 0$ (+), $\lambda = 0.2$ (\square), $\lambda = 1$ (\diamond), $\lambda = 2$ (\triangle), $\lambda = 5$ (*).

5. Concluding remarks

We have developed a computer simulation for concentrated emulsion flow that can describe the steady-state rheology and microstructure. Only modest computational resources are needed. Numerical results were presented for the transient and steady-state rheology of concentrated emulsions with volume fractions up to 30% and dispersed-phase viscosity ratios in the range $0 \leq \lambda \leq 5$. A complex viscoelastic shear-thinning rheology is predicted and related to detailed microstructural features. Drop deformation and alignment in the flow direction result in the formation of an anisotropic microstructure that reduces the collision cross-section of the drops and allows them to glide past each other with less resistance; low shear stresses and large normal stresses are the macroscopic manifestation of these phenomena. The viscosity of an emulsion was found to be a moderate, approximately linear, function of the dispersed-phase volume fraction, at least up to $\phi = 30\%$, unlike the sharply increasing

viscosity of suspensions of rigid particles or undeformed drops. The deformation of emulsion drops eliminates the geometrical blockages that cause rigid particles to form large clusters.

The accuracy of the numerical procedure has been tested for convergence with respect to the number of drops used in each unit cell and the number of boundary elements used on each drop surface. The simulation has also been tested against several published and unpublished results. We are unaware of experimental results suitable for a comparison. Further numerical work should include an improved description of the drop interfaces, including an improved curvature calculation and a collocation mesh capable of adaptive reconnections. Eventually, a detailed numerical simulation that incorporates drop breakup and coalescence may become feasible.

Hopefully, the work presented in this article will provide a useful tool for developing and testing simplified microphysical models of concentrated emulsion rheology. The predictions of simplified models should help to design an interesting experimental study. Proceeding in this way, a firm basis for understanding and predicting emulsion flow should be possible.

M.L. was supported by a NATO-NSF Fellowship. The computations were supported in part by the SERC CSI grant GR/H57585 and in part by the DTI LINK programme on colloids.

REFERENCES

- ARONSON, M. P. & PETKO, M. F. 1993 Highly concentrated water-in-oil emulsions: influence of electrolyte on their properties and stability. *J. Colloid Interface Sci.* **159**, 134–149.
- BATCHELOR, G. K. 1970 The stress system in a suspension of force-free particles. *J. Fluid Mech.* **41**, 454–570.
- BEENAKER, C. W. J. 1986 Ewald sum of the Rotne-Prager tensor. *J. Chem. Phys.* **85**, 1581–1582.
- BENALI, L. 1993 Rheological and granulometric studies of a cutting oil emulsion. I. The effects of oil concentration. *J. Colloid Interface Sci.* **156**, 454–461.
- BENTLEY, B. J. & LEAL, L. G. 1986 An experimental investigation of drop deformation and breakup in steady, two-dimensional linear flows. *J. Fluid Mech.* **167**, 241–283.
- BRADY, J. F. & BOSSIS, G. 1988 Stokesian dynamics. *Ann. Rev. Fluid Mech.* **20**, 111–157.
- BRUIN, R. A. DE 1989 Deformation and breakup of drops in simple shear flows. PhD thesis, Eindhoven.
- CHOI, S. J. & SCHOWALTER, W. R. 1975 Rheological properties of nondilute suspensions of deformable particles. *Phys. Fluids* **18**, 420–427.
- D'ARRIGO, J. S. 1986 *Stable Gas-in-Liquid Emulsions*. Elsevier.
- DAS, A. K., MUKESH, D., SWAYAMBUNATHAN, V., KOTKAR, D. D. & GHOSH, P. K. 1992 Concentrated emulsions. 3. Studies of the influence of continuous-phase viscosity, volume fraction, droplet size, and temperature on emulsion viscosity. *Langmuir* **8**, 2427–2436.
- DOI, M. & OHTA, T. 1991 Dynamics and rheology of complex interfaces. I. *J. Chem. Phys.* **95**, 1242–1248.
- FRIBERG, S. E. (Ed.), 1976 *Food Emulsions*. Marcel Dekker.
- GRACE, H. P. 1982 Dispersion phenomena in high viscosity immiscible fluid systems and application of static mixers as dispersion devices in such systems. *Chem. Engng Commun.* **14**, 225–277.
- HINCH, E. J. & ACRIVOS, A. 1980 Long slender drops in a simple shear flow. *J. Fluid Mech.* **98**, 305–328.
- KENNEDY, M. R., POZRIKIDIS, C. & SKALAK, R. 1994 Motion and deformation of liquid drops, and the rheology of dilute emulsions in simple shear flow. *Comput. Fluids* **23**, 251–278.
- LI, X., ZHOU, H. & POZRIKIDIS, C. 1995 A numerical study of the shearing motion of emulsions and foams. *J. Fluid Mech.* **286**, 379–404.
- LISSANT, K. J. (Ed.) 1984 *Emulsions and Emulsion Technology*, Part III. Marcel Dekker.

- MO, G. & SANGANI, A.S. 1994 Method for computing Stokes flow interactions among spherical objects and its application to suspensions of drops and porous particles. *Phys. Fluids* **6**, 1637–1652.
- MULDOWNEY, G.P. & HIGDON, J.J.L. 1995 A spectral boundary element approach to three-dimensional Stokes flow. *J. Fluid Mech.* **298**, 167–192.
- OTSUBO, Y. & PRUD'HOMME, R.K. 1994 Rheology of oil-in-water emulsions. *Rheol. Acta* **33**, 29–37.
- PAL, R. & RHODES, E. 1985 A novel viscosity correlation for non-Newtonian concentrated emulsions. *J. Colloid Interface Sci.* **107**, 301–307.
- PAL, R. & RHODES, E. 1989 Viscosity/concentration relationships for emulsions. *J. Rheol.* **33**, 1021–1045.
- POZRIKIDIS, C. 1992 *Boundary Integral and Singularity Methods for Linearized Viscous Flow*. Cambridge University Press.
- POZRIKIDIS, C. 1993 On the transient motion of ordered suspensions of liquid drops. *J. Fluid Mech.* **246**, 301–320.
- PRINCEN, H.M. & KISS, A.D. 1989 Rheology of foams and highly concentrated emulsions: IV An experimental study of the shear viscosity and yield stress of concentrated emulsions. *J. Colloid Interface Sci.* **128**, 176–187.
- RALLISON, J.M. 1981 A numerical study of the deformation and burst of a drop in general shear flows. *J. Fluid Mech.* **109**, 465–482.
- RALLISON, J.M. & ACRIVOS, A. 1978 A numerical study of the deformation and burst of a drop in an extensional flow. *J. Fluid Mech.* **89**, 191–209.
- ROETTING, O. & HINRICHSSEN, G. 1994 Blends of thermotropic liquid crystalline and thermoplastic polymers: a short review. *Adv. Polymer Tech.* **13**, 57–64.
- SCHWARTZ, L.W. & PRINCEN, H.M. 1987 A theory of extensional viscosity for flowing foams and concentrated emulsions. *J. Colloid Interface Sci.* **118**, 201–211.
- SJÖBLM, J. (Ed.), 1992 *Emulsions – A Fundamental Approach*. Kluwer.
- TEH, J.W., RUDIN, A. & KEUNG, J.C. 1994 A review of polyethylene-polypropylene blends and their compatibilization. *Adv. Polymer Tech.* **13**, 1–23.
- YIANTSIOS, S.G. & DAVIS, R.H. 1991 Close approach and deformation of two viscous drops due to gravity and van der Waals forces. *J. Colloid Interface Sci.* **144**, 412–433.
- ZHOU, H. & POZRIKIDIS, C. 1993 The flow of ordered and random suspensions of two-dimensional drops in a channel. *J. Fluid Mech.* **255**, 103–127.
- ZHOU, H. & POZRIKIDIS, C. 1994 Pressure-driven flow of suspensions of liquid drops. *Phys. Fluids* **6**, 80–94.
- ZINCHENKO, A.Z. 1983 Calculations of the effectiveness of gravitational coagulation of drops with allowance for internal circulation. *Prikl. Mat. Mech.* **46**, 58–65.
- ZINCHENKO, A.Z. 1984 Effect of hydrodynamic interactions between the particles on the rheological properties of dilute emulsions. *Prikl. Mat. Mech.* **48**, 198–206.